Plasma Electrode Dielectric Barrier Discharge: Development, Characterization and Preliminary Assessment for Large Surface Decontamination

Fellype Do Nascimento, Augusto Stancampiano, Kristína Trebulová, Sébastien Dozias, Jan Hrudka, František Krčma, Jean-Michel Pouvesle, Konstantin Georgiev Kostov, Eric Robert

Plasma electrode dielectric barrier discharge: development, characterization and preliminary assessment for large surface decontamination

Fellype do Nascimento[1], Augusto Stancampiano[2], Kristína Trebulová[3], Sébastien Dozias[2], Jan Hrudka[4], František Krčma[3], Jean-Michel Pouvesle[2], Konstantin Georgiev Kostov[1], and Eric Robert[2]*

[1] Faculty of Engineering in Guaratinguetá, São Paulo State University–UNESP, Guaratinguetá 12516-410, Brazil

[2] GREMI, UMR 7344, CNRS/Université d'Orléans, 45067 Orléans, France

[3] Brno University of Technology, Faculty of Chemistry, Purkyňova 118, 612 00 Brno, Czech Republic

[4]University of Chemistry and Technology Prague, Technická 5, Dejvice, 166 28 Praha 6, Czech Republic

* Corresponding author: eric.robert@univ-orleans.fr

Abstract

The paper gives the detailed information about a newly developed plasma system applicable for conductive target non-thermal plasma indirect treatment. High voltage microsecond duration pulses delivered in the kHz range are used to ignite a discharge in a glass funnel vessel flushed with argon and equipped with a needle electrode. An air dielectric barrier discharge (DBD) can subsequently be generated if a grounded grid is set a few millimeters apart from the thin glass plate constituting the funnel base, in the funnel-DBD setup. Thus, this air DBD operates with its powered electrode consisting in the transient argon streamer discharge spreading inside the funnel and over the glass plate. This "plasma electrode DBD" is characterized using time-resolved ICCD imaging together with voltage and current probes. This work reports for the first time the funnel-DBD proof of concept operation and its potentialities for large surface decontamination. Argon and air plasma temporal and spatial development is documented and analyzed while electrical characterization using Lissajous plots provide key information on the power and capacitances of the funnel-DBD setup. It is reported that the funnel-DBD operates as a large surface and low power discharge. As with any air-DBD plasma, the modulation of the power density delivered across the air-DBD, processed with changing the pulse repetition rate, results in the control of the ozone concentration. Beyond the plasma electrode-DBD development and characterization, the main motivation of this work is the treatment of conductive samples with the perspective of large surface decontamination. Preliminary demonstrations of the bacterial and yeast inhibition are thus reported for *in vitro* cultivations through indirect treatment with the funnel-DBD delivering reactive nitrogen and oxygen species.

Keywords: dielectric barrier discharge; surface decontamination; ICCD imaging; streamer discharge; plasma electrode

I Introduction

Nowadays, surface modification and decontamination by atmospheric pressure plasmas are well established technologies. By tailoring the surface properties, it becomes possible to improve adhesion between polymers and other materials, enable printing or coating processes, enhance surface energy, introduce functional groups, reduce friction or wear, increase resistance to chemicals or environmental degradation, enable specific biological interactions, inactivate germs and induce tissue healing among other possibilities. These modifications pave the way for advancements in industries such as automotive, aerospace, packaging, electronics, and healthcare, as well as stimulate the continuous development of novel atmospheric pressure plasma sources.

Atmospheric pressure plasma jets (APPJs) are low-cost devices that emerged as an alternative to the conventional dielectric barrier discharge (DBD) systems that are well suited for processing plane samples, but inadequate for treating complex 3D structures. Typically, in an APPJ electric discharge is ignited in a noble gas that flows through a dielectric channel and the resulting plasma is ejected into the surrounding environment (usually ambient air), forming a plasma plume [1]. The plasma plume is the discharge region, driven by ionization waves, expanding at the outlet of the capillary channel. As the plasma stream propagates into the surrounding atmosphere [2], it interacts with the ambient molecules creating reactive oxygen and nitrogen species (RONS) that upon reaching a target can induce surface modification [3, 4] and decontamination [5] effects. The plasma jets are characterized by diverse geometries and electrode configurations and can be driven by pulsed DC, AC, RF and microwave sources using different operating parameters, which makes them very versatile [1, 4]. In addition, the APPJs normally generate a several cm-long plasma plume [6] that can be easily adapted to treat irregular 3D objects and internal surfaces of narrow tubes or cavities [5]. Moreover, the gas temperature can be kept quite low (under 40 C^o in some cases), which makes the plasma jets suitable for medical applications and treatment of thermosensitive materials [4]. All these beneficial properties of the plasma jets led to intense research in the last two decades resulting in the development of many different APPJ systems [1, 5].

However, the plasma jet application in material surface modification and decontamination presents its challenges. For instance, for many technological applications achieving uniform treatment across extensive areas, maintaining treatment conditions, and ensuring process scalability, are among the issues that need to be addressed. An inherited drawback of most common APPJs is the fact that

the plasma plume diameter is determined by the inner diameter of the dielectric tube or capillary [1, 6, 7], (normally few mm), which combined with the short lifetime of the reactive species results in a limited treatment zone [8]. In fact, the size of the modified area of an atmospheric plasma jet is a dynamic parameter that can be controlled and adjusted to a certain extent through various means, including jet exit nozzle design, gas flow rate, discharge operating parameters, and distance to the target [9]. Understanding and optimizing these factors is crucial for achieving the desired outcome in plasma jet applications. Yet, the substrate area altered by a single plasma jet is typically limited to a few cm^2 [9, 10]. Moreover, within the plasma-treated surface the degree of material modification/decontamination is not uniform, being more intense at the center (where the plasma jet hits the target) and less pronounced at the edges [11]. As shown in [12] by using proper shielding gas the plasma-modified area can be further extended by ~20% , but this gain is at the expense of introducing new components and increasing the system complexity.

Of course, it is possible to achieve a larger modified area by utilizing scanning or rastering techniques, where the plasma jet and/or the target are systematically displaced. By employing controlled movement patterns and multiple passes, a bigger surface can be effectively covered by the jet. For instance, in [13] the authors report on an especially designed system for simultaneous jet rotation and tilting, which provides a uniform decontamination over a circular area of ~20 cm^2. However, in general the jet/target scanning techniques result in excessive time of treatment and require sophisticated jet/target mechanical systems, which aggregates additional process costs. To deal with this in some excitation schemes like in [14-18] a long (up to 10-cm), brush-type plasma jet was generated in a narrow (typically few mm) gas duct. This linear plasma plume combined with a one-dimensional target movement, can provide uniform treatment over a large rectangular area [14]. Yet, as shown in [15,17] the discharge is prone to instabilities that perturb plasma plume distribution along the gas duct thus compromising the treatment uniformity. Although some of these devices operate with Ar [15, 18] and air [16] the brush-type plasma jets require excessively high gas flow rates (tens of l/min).

Therefore, besides the target/jet manipulation [13], other techniques were attempted to remedy the plasma jet's disadvantage of having a small treatment area. For example, to increase plasma jet diameter some works rely on using wide dielectric tubes [19] with different geometry [20, 21]. However, by these means a stable plasma plume can be generated only in He gas flow within tubes with inner diameter up to about 2 cm. Some authors proposed obtaining one bigger plasma column by cooperative merging of several small He plasma jets [22, 23]. Alternatively, in [24] several radial streams of He gas were directed perpendicularly to a vertical He plasma jet and consequently ignited

thus creating a wider plasma region close to a target. A common disadvantage of all these methods is that the device´s operation requires high flow rates (~10 L/min) of Helium.

It was reported that the treatment area of plasma jets could be increased by using high discharge frequency [20, 25] or different electrode arrangements [26]. In these two cases, the plasma jet power was enhanced leading to production of more reactive species and as a result, the plasma modification effect extended over a bigger area. However, at the same time the thermal load to the target also tends to increase making it inappropriate for thermosensitive samples.

To deal with the jet's small diameter, some work employed arrays or matrices of many plasma jets [27-32]. For instance, in [32] a matrix of 52 He plasma jets was reported and tested for bacterial inactivation over a large surface. In general, these devices were able to provide an extension of plasma modification effect over areas of tens of cm^2. However, operating many jets in parallel results in high total gas flow and difficulties controlling the gas flow rate of each individual jet. Moreover, due to the complex interaction between the individual jets in a plasma array [27] some jets are deflected [28, 29] or even extinguished [30], which makes it hard to ensure a uniform surface modification. To overcome these issues researchers are exploring special geometries of plasma jet arrays [33] and different electrode configurations [31]. In summary, although some advances have been achieved it is still a considerable challenge to construct and optimize an atmospheric plasma jet system capable of uniform surface modification over a large area.

Therefore, alternative solutions to the above discussed issue have been pursued. In this sense, the authors in [34] proposed a simple “corona-like” atmospheric pressure plasma source operating in a pin-to-plate geometry. It consisted of a pin electrode centered inside the narrow part of a quartz funnel. The latter was installed vertically with its wide orifice facing down. A grounded metallic plate covered by a glass was placed a few mm under the funnel conical exit. The system was fed with Ar gas introduced through the funnel´s narrow part. Plasma was generated in the form of multiple filaments that emerged from the pin electrode, propagated along the funnel wall until reaching the glass substrate. The reactive species generated by the plasma are trapped inside the conical horn [35] and therefore can efficiently modify a dielectric target placed on the glass. The device was able to perform uniform surface modification over the entire area covered by the funnel exit without any target/jet manipulation [34]. In addition, the device is scalable, i.e., the plasma treated area can be increased by simply choosing a funnel with larger exit nozzle and adjusting the process parameters. Moreover, both sides of planar samples were modified simultaneously [36] and entire 3D objects (like seeds or small samples) that are placed inside the funnel can be treated on all sides [37]. However, this system also

has shortcomings, because it is not appropriate for treating conductive or liquid samples due to the risk of arc formation. Here we report on a modification of the aforementioned system, which led to development of an innovative device with a “plasma electrode” suitable for treatment of conductive targets.

This paper is organized as follows. The device setup and characterization methods are described in the Experimental setups section. The obtained results together with discussion are presented in the next section. Preliminary tests on microbial inactivation over large areas are also reported here. Finally, the conclusions and suggestions for future works are outlined in the Conclusions.

II Experimental setups

II- 1 - Funnel and funnel-DBD devices

An atmospheric pressure plasma device with conical shape was studied in this work. The different device configurations used in this work are depicted in Figure 1 and mainly consist of a quartz funnel with a needle electrode centered inside it. The diameter of the needle is 2 mm and the full angle of the needle tip is 25°. This needle was the same one used for all the data documented in this work. Both parts are joined through a plastic connector, which is also used for admitting argon (Ar) gas into the system. The funnel straight part has external and internal diameters equal to 9 mm and 7 mm, respectively, and a height of 80 mm. The funnel terminates with a conical part, which has a maximum opening of 80 mm in diameter, thickness of 1 mm and height of 65 mm. In the original configuration of the funnel-based device presented in [34], the tip of the needle electrode is positioned inside the funnel pipe at a height (h) of 75 mm. Therefore to produce a discharge in the funnel it is necessary to place a dielectric plate very close (few mm) to the base of the cone, like depicted in Figure 1(a). The use of a grounded metallic plate under the dielectric plate facilitates the discharge ignition and also increases the discharge power. When argon gas is injected inside the funnel and an electrical voltage of the order of a few kV is applied to the needle electrode a filamentary discharge is ignited. If the tip of the needle electrode is far from the glass plate below the funnel exit, the discharge filaments emerge from the tip electrode and propagate along the internal surface of the cone wall [34, 36]. Once the discharge filaments reach the dielectric substrate, they spread radially inward over the surface and cover the entire area under the cone. Thus, such plasma can be used to treat materials inside the funnel.

Due to limitations of the device operation (risk of transition to arc discharge when the material to be treated is conductive, as is the case of agar, for example), a modification was made to the device original configuration so that it started operating like a parallel plate DBD device. Two modifications were necessary for that: a reduction in the height h to 55 mm or less and a replacement of the metallic plate beneath the glass plate (dielectric permittivity of about 5) by a circular metallic grid, as depicted in Figure 1(b-d). Both the metallic holder in Figure 1(d) and the new metallic grid are grounded through a 100 Ω resistor. This configuration will be called funnel-DBD from now on. The grid used in the experiments has a circular shape. It is composed of five concentric metal wires whose diameters are 14 mm, 28 mm, 43 mm, 58 mm and 72 mm and thickness is 1 mm.

By reducing the height h, the discharge occurs directly from the needle to the glass plate instead of running along the internal funnel surface. Then, when the discharge reaches the plate it forms filaments that spread over the surface under the funnel exit. The spreading diameter of the filaments changes depending on the gas flow rate.

Since the discharge filaments are conductive channels, the plasma on the glass plate acts as a temporary electrode with an area proportional to the plasma coverage of the surface. Thus, leaving a small gap between the glass plate and the metal grid it is possible to produce a DBD-like air discharge between the two parts. In this way, the reactive species generated in such secondary discharge can be used for surface decontamination.

Figure 1(a) shows the scheme for studying the development of the discharge inside the funnel. In this case, the device was placed over a glass plate with a 0.5 mm gap between them. The needle tip to glass plate gap (h) was 55 mm. The scheme shown in Figure 1(a) was used for electrical characterization and ICCD imaging of the discharge streamers propagating over the internal surface of the cone.

Figures 1(b) to 1(d) show the setups used to investigate the funnel-DBD configuration. In Figure 1(b) it is shown the schematics for fast imaging diagnostics together with the current measurements employed. In Figure 1(c) is presented the scheme for ozone production measurements. Figure 1(d) shows the setup used to perform the electrical characterizations of the device as well as for evaluation of the production of reactive oxygen and nitrogen species (RONS) and biological assays. The value of h was fixed at 16 mm in all experiments using the schemes in Figures 1(b) to 1(d), except for the electrical characterization for which multiple h values were investigated.

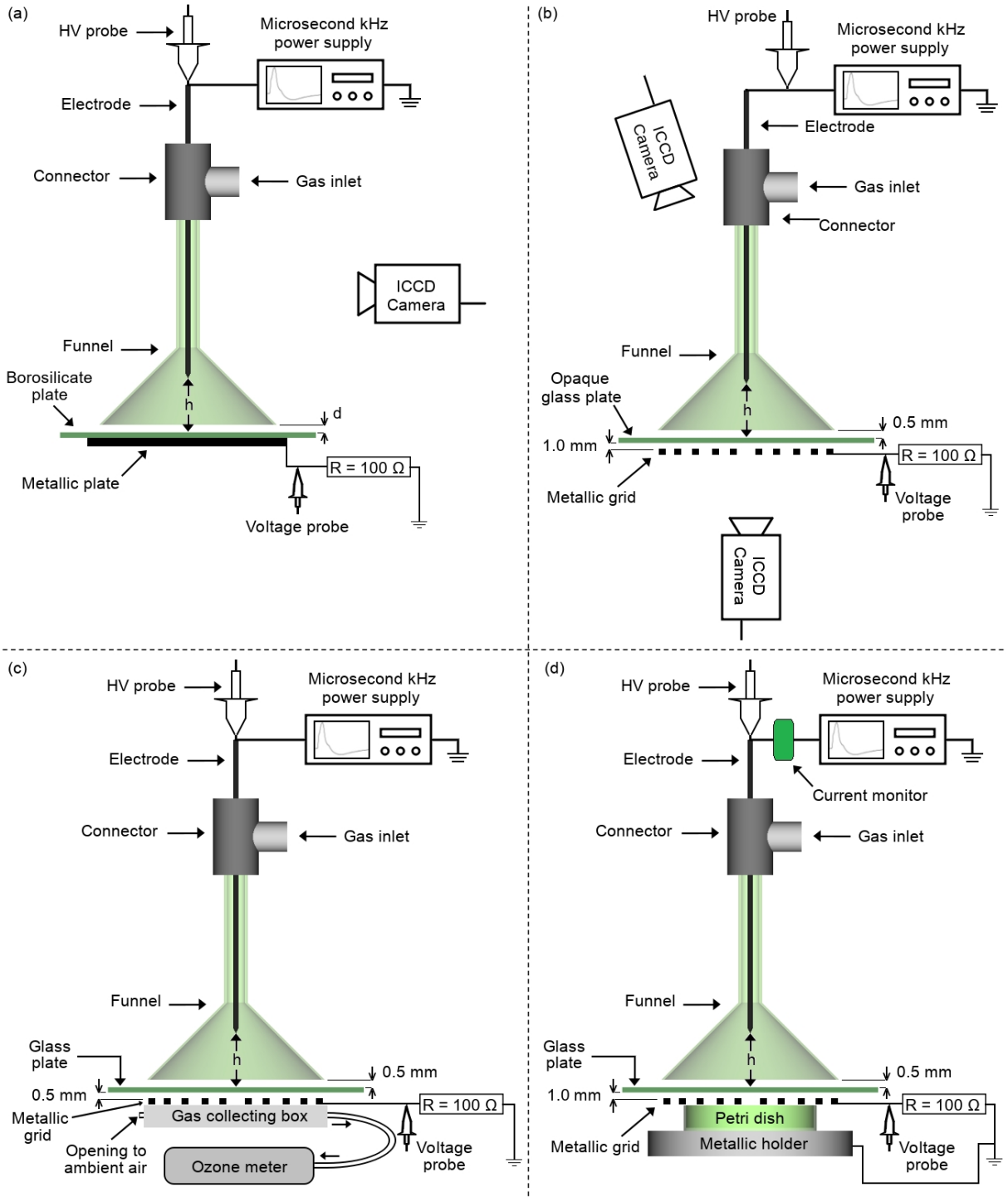

Figure 1: Schematics of experimental arrangements for: (a) ICCD imaging of the funnel discharge with the metallic plate only, (b) ICCD imaging of the funnel-DBD, (c) ozone production measurements in the funnel-DBD configuration and (d) electrical characterization of funnel-DBD and biological assays.

In order to produce the plasma discharges a voltage source developed by GREMI was used as the power supply [38]. The voltage waveform produced by this equipment is a Gaussian-like pulse with ~2μs full width at half maximum (FWHM). The rise time of the voltage pulse is about one microsecond, and the energy per pulse is typically of a few hundreds of μJ depending on the voltage amplitude in the range of 5 to 15 kV. For 10 kHz pulse repetition rate and 10 kV peak amplitude, the power delivered by the generator is about 20 W. It can be operated in both positive and negative polarities in a pulse repetition rate ranging from single shot to 20 kHz and voltage amplitude up to 20 kV. High voltage measurements were carried out using a 1000:1 voltage probe from Tektronix (model P6015A). Input current was measured using a current monitor from Pearson (model 6585). The discharge current was obtained by measuring the voltage across the shunt resistor (100 Ω) that was in series with the metallic grid. Waveforms were recorded in an oscilloscope from Tektronix (model DPO4104B). The Ar flow rate was kept constant at 1.0 standard liter per minute (slm) in all experiments.

The electrical characterization of the funnel-DBD was carried out in order to obtain the power injected into the system, the total power dissipated in the plasma discharges, the power per unit area in the region between the glass plate and the metallic grid, and also the system capacitance (gas gap plus dielectric, C_{g+d}). All these parameters were analyzed for different operating frequencies of the voltage source and for h varying of 6, 30 and 55 mm.

In addition to the funnel-DBD configuration, electrical parameters were also measured for a conventional DBD system, formed by a solid disc electrode, 5.6 cm in diameter that replaced the funnel and was in contact with the top side of the glass plate.

The C_{g+d} values were obtained using the method described by Pipa et al [39]. In order to do that, the temporal evolution of the charge flowing through the system was obtained by numerical integration of the measured current waveforms. After that, a q–V plot was generated and the C_{g+d} value was extracted from the slope of the q–V curve linear segment corresponding to the phase without discharge ignition. When using the solid electrode, it was possible to extract also the value of the dielectric capacitance (C_d) from the linear segment of the q–V curve that corresponds to the phase with discharge ignition. An estimation for the C_d value using the funnel-DBD configuration was also performed. This was assessed by linear fitting of the Lissajous plot segment during the temporal window when the air gap is not yet ignited but the argon plasma covers the glass plate upper surface.

II-2 - Imaging of plasma discharges

Fast imaging diagnostics were carried out using an ICCD camera from Teledyne Princeton Instruments (model PI-Max 3). The ICCD was synchronized with the voltage pulse delivered by the high voltage power supply. This was performed for the setup shown in Figure 1(a) in order to study the development of the discharge over the internal surface of the funnel. In this experiment, the dielectric plate was made of 1 mm thick borosilicate glass. Fast imaging of the discharges in the funnel-DBD configuration was performed in two ways: with the ICCD camera placed above the cone of the funnel, like depicted in Figure 1(b), in order to analyze the development of the needle to glass plate discharge, and with the ICCD camera below the metallic grid for imaging the discharge below the glass plate. This latter configuration was used to image the air DBD generation. A 2.8 mm thick opaque soldering glass plate was used as the glass plate to filter the argon plasma emission from inside of the funnel. It was observed that the optical transmission of this opaque plate is extremely low, completely blocking the detection of argon plasma emission above the plate by the ICCD camera positioned below the plate. As the ICCD imaging was performed with this 2.8 mm thick glass plate, the electrical characterization and ozone measurement, documented in this work, with the funnel-DBD device were also processed with this same glass plate acting as the dielectric plate of the DBD discharge.

II-3 - Measurement of ozone and other reactive species

The amount of ozone (O_3) produced within the discharge between the glass plate and the metallic grid was evaluated quantitatively and as a function of time using the setup shown in Figure 1(c). In order to do that, a gas collecting box was placed right below the metallic grid. That collecting box is connected to an ozone meter (In-2000 locon ozone analyzer) through a flexible polytetrafluoroethylene tube. The ozone meter continuously sucks the gas from the collecting box with a flow rate of 1.5 slm to an absorption cell to quantify the ozone concentration. The ozone measurement was performed as the air DBD discharge obviously generates ozone which may play an important role for decontamination applications and to characterize the performance of the device for ozone production with respect to the injected power density.

The RONS production was evaluated for nitrite (NO_2), nitrate (NO_3) and hydrogen peroxide (H_2O_2). For this purpose, the petri dish shown in Figure 1(d) was filled with 15 mL of distilled water, placed under the metallic grid and exposed to indirect plasma treatment. Then, after plasma exposure, test strips (Quantofix), for detection of NO_2, nitrate NO_3 and H_2O_2 were used to evaluate the amount of such species present in the water.

II-4 - Surface decontamination assays

The setup shown in Figure 1(d) was employed in tests with KI-starch agar for a primary evaluation of the possibility of using the reactive species produced within the discharge that occurs between the glass plate and the metal grid for surface decontamination. For this purpose, a petri dish filled with KI-starch agar was placed under the metallic grid and exposed to indirect plasma treatment for 1-3 min time intervals. For the biological assays 2 different microbes were chosen: a gram-negative bacteria *Escherichia coli* (*E. coli*) as a model prokaryotic representative and a yeast *Candida glabrata* (*C. glabrata*) as a model eukaryotic representative. Biological assays with *E. coli* and *C. glabrata* were performed in a similar way. Petri dishes with inoculated microbial culture were placed under the metallic grid and exposed to indirect plasma treatment. The exposure time used for treating *E. coli* was 60 seconds. *C. glabrata* was exposed to different treatment times ranging from 5 to 20 minutes.

Biological assays with *C. glabrata* were carried out not only with the quartz funnel, with the dimensions mentioned above (to be referred to as “small funnel” in the results section), but also with a glass funnel whose pipe dimensions were bigger, with external and internal pipe diameter of 9 mm and 7 mm, respectively, and a height of 120 mm. The cone has a maximum opening of 130 mm in diameter, thickness of 2 mm and height of 110 mm (to be referred to as “big funnel” later on). In the tests performed using the small funnel the device was operated with a peak voltage of 7.0 kV and in those carried out with the big funnel the peak voltage was 8.6 kV, with positive polarity in both cases. The modulation of the peak voltage amplitude was processed to achieve the same 9 W input power with both funnel setups. The pulse repetition rate was kept constant at 8 kHz in all the biological assays.

For testing of the antimicrobial activity, the yeast strain *C. glabrata* CCM 8270 was used, supplied by the Czech Collection of Microorganisms [40]. The inoculum was prepared in the YPD (Yeast extract Peptone -Dextrose/Glucose) liquid medium and cultivated for 24 h at the temperature 37 °C in a tempered incubator with shaking. The prepared 24 hour inoculum was diluted to the initial cell concentration of 10^6 CFU/ml.

Solid YPD medium was poured evenly into plastic Petri dishes with the diameter of 90 mm so that the agar layer was about 2 mm. The volume of 100 µl of prepared culture *C. glabrata* was inoculated on these agar plates.

Inoculated agar plates were exposed to the plasma immediately after the inoculation. Each Petri dish was treated individually. Treatment times chosen for the application were 5, 10, 15 and 20 minutes. The distance of the treated surface from the device grid was 5 mm. The temperature of the

treated surface did not exceed 50 °C (estimated using reversible thermosensitive stickers). The samples treated with the selected discharges were subsequently cultivated in a thermostat for 48 hours at the temperature of 37 °C. All measurements were replicated twice, and control samples (without the plasma treatment) were evaluated. All Petri dishes were photographed after 24 hours and 1 week. Then, the size of the inhibited area was evaluated in cooperation with the HexTech s.r.o. using the software Aurora.

Aurora uses artificial intelligence and principles of machine learning to separate the parts of our interest from the input material by classifying pixels according to their spectral intensities. Thanks to this step it distinguishes agar and the environment from the microbial culture. The output is the percentage of the area covered by the microbial culture [41]. This raw data is turned into inhibition efficiency by subtracting the area covered by the yeast of the treated sample from the area covered by the yeast in the control sample.

III Results

III-1 Physical characterization of funnel and funnel-DBD devices

III-1 a Funnel device

In this first section, the funnel device developed in [34] was used in a baseline configuration (Figure 1a). The main motivation was to operate the device using the microsecond high voltage pulse delivered by the lab-developed GREMI power supply [38] and to perform fast imaging characterization of the discharge ignition and propagation inside the funnel. Figure 2a presents the voltage measured on the needle electrode and the current deduced from the voltage drop measurement across the 100 Ω resistor. If connected to a pure resistive load, the power supply delivers a 2 µs FWHM, Gaussian-like 8 kV peak amplitude voltage pulse with the pulse repetition rate set at 2 kHz. As shown in Figure 2a, this voltage pulse is drastically modified when the funnel device discharge is ignited. At the time of 1.4 µs, a significant voltage drop is measured, reducing the voltage amplitude to about 5 kV. This voltage drop coincides with a strong current peak measured across the resistor. Following this current peak, a negative current peak of lower amplitude is measured by the end of which the voltage amplitude is stable before gradually decreasing. Another short duration current spike is also detected around 800 ns. The voltage and current waveforms exhibit the same features for other peak voltage amplitude and pulse repetition rate imposed from the power supply. Nevertheless, the different current peak timing and amplitude, and the voltage drop amplitude are modified. Time resolved ICCD imaging depicted in Figure 2b reveals the links between the current waveform and the plasma discharge development. The

first current spike around 800 ns occurs simultaneously with the ignition of the corona discharge at the tip of the needle electrode. The plasma immediately expands towards the funnel inner surface and experiences a very fast propagation along this surface, while the current is gradually increasing from about 1 to 1.4 µs. The current peak timing coincides with the plasma front touching the glass plate.

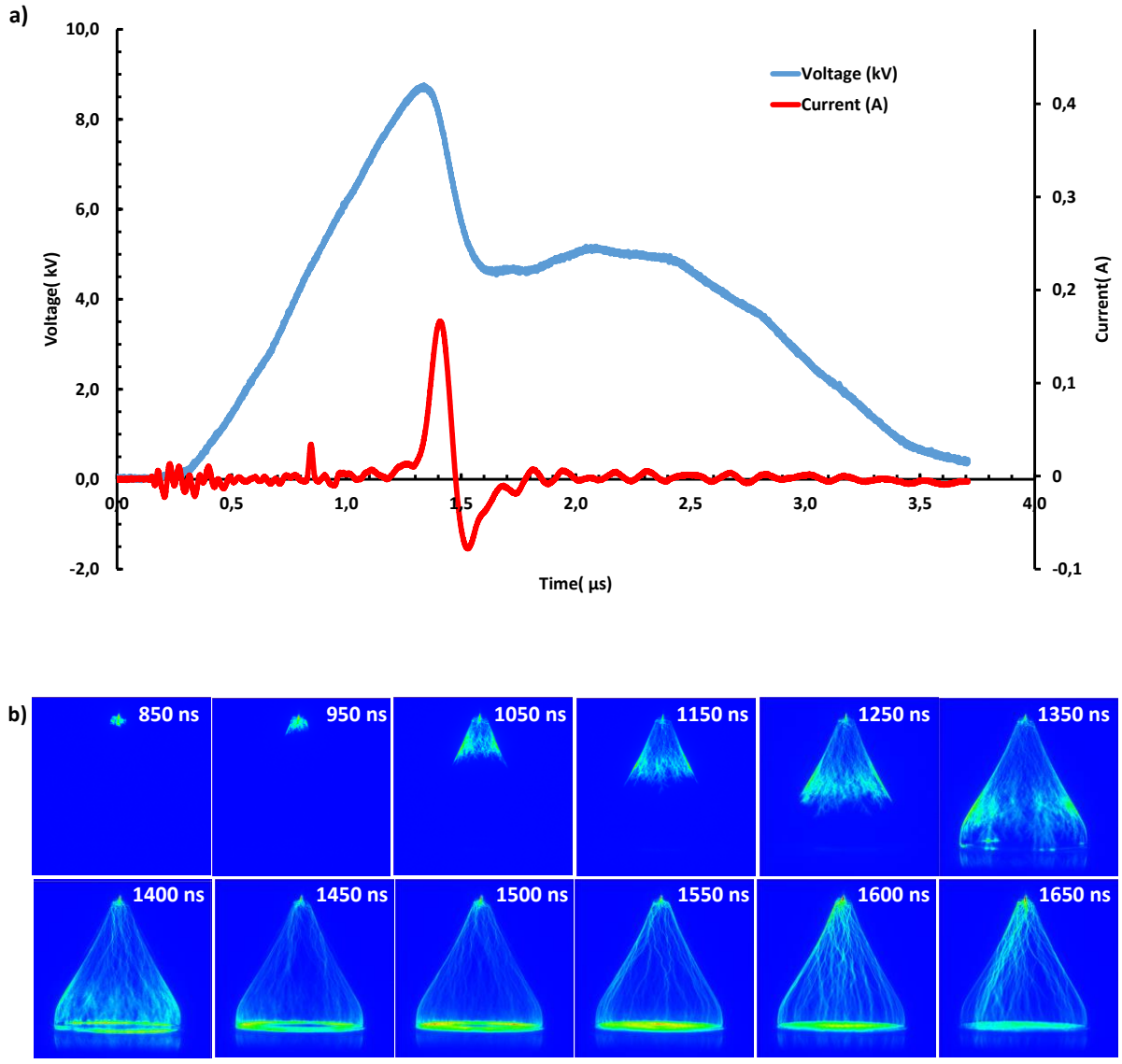

Figure 2: (a) voltage/current waveforms. (b) ICCD imaging lateral view (time in ns on the top right of frames: gating time is 20 ns, each image is averaged over 50 discharges)

So following the corona discharge ignition, the argon plasma develops as a sliding discharge whose velocity, inferred from ICCD images, is about 1.4 10^7 cm/s. This velocity amplitude is typically of the same order as that measured during ionization wave propagation in kHz plasma jets powered by the same power supply and with the same voltage amplitude [38, 42]. ICCD images captured from 1450

to 1650 ns reveal the expansion of the plasma on the upper surface of the glass plate from the outer to the center. This plasma sliding phase on the glass plate occurs during the negative current peak while a positive voltage is still imposed on the needle tip. As the discharge contacts with the bottom plate, the upper surface of this plate is positively charged. Charge neutralization occurs across this plate connected in series with the 100 ohm grounded resistor. This results in the negative polarity current peak measured in Figure 2a) around 1.5 µs.

The main current pulse is associated with the plasma propagation along the inner funnel surface from the needle tip to the glass plate. If the gap from the needle tip to the glass surface is reduced, the discharge reaches the glass plate quicker and can be ignited for a lower peak voltage amplitude. Nevertheless, when setting the needle tip closer and closer to the glass plate, the distance from the needle tip to the lateral funnel surface increases. This induces the development of a streamer directly connecting to the bottom plate, then leading to a strong current and much less spreading over the glass plate. This is not the best operation mode of the funnel device if large surface plasma on the bottom plate is desired. Same kind of behavior is also observed when keeping the needle at a fixed position with respect to the glass plate but with increasing the pulse repetition rate, as documented in the next paragraph.

- Influence of cone base- glass plate gap and pulse repetition rate

a)

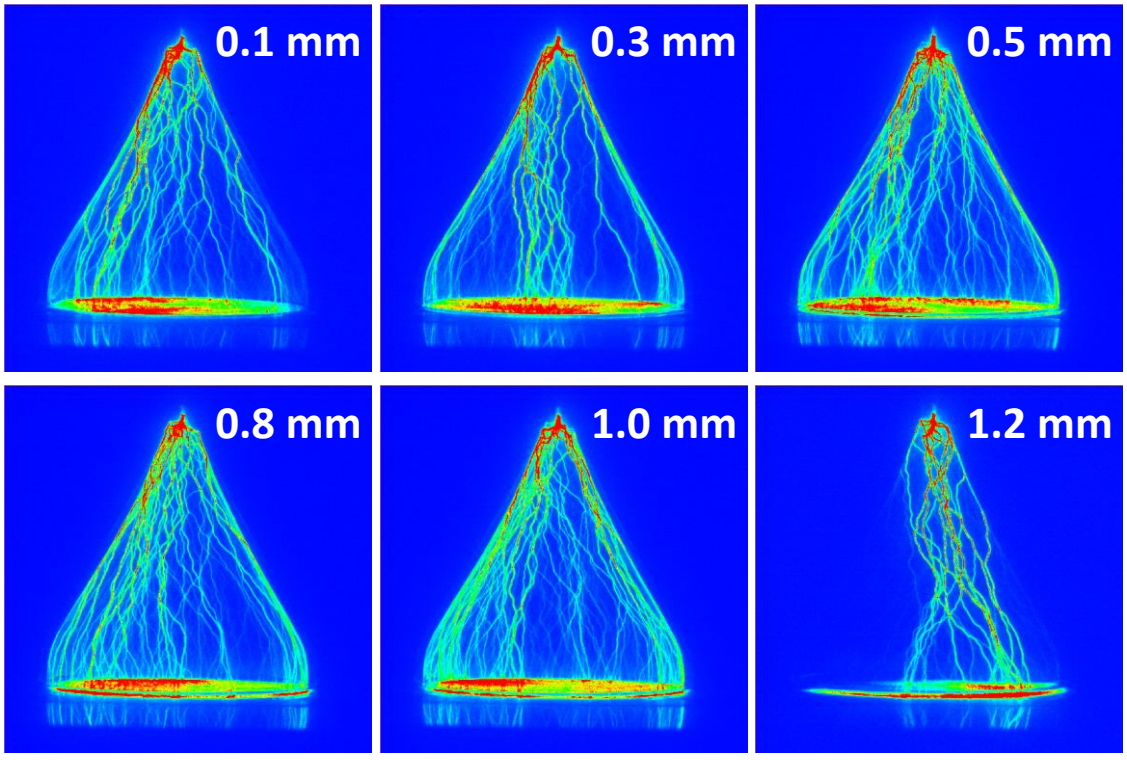

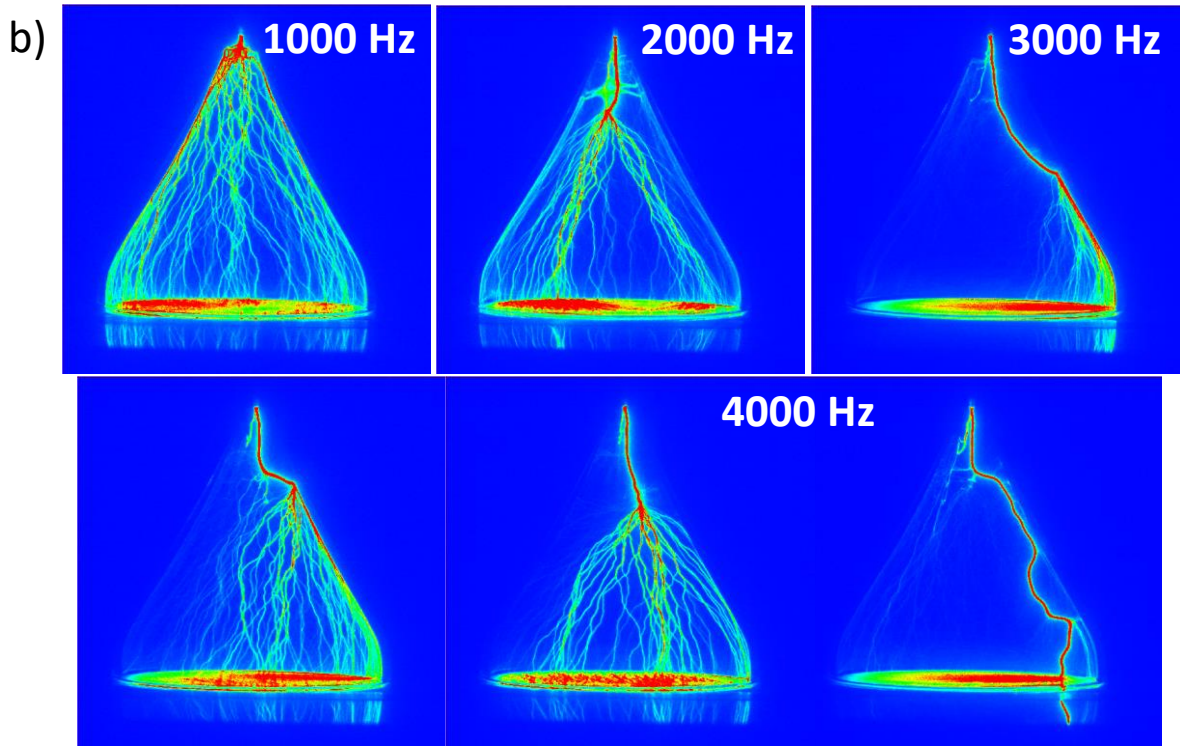

Figure 3: Influence of (a) cone base-glass plate gap (gap in mm on top right of each frame) and (b) pulse repetition rate on the discharge development inside the funnel. Three images for the 4000 Hz operation are documented to enlighten the arbitrary transition between different discharge propagation modes. Gating time is 5 µs, images are single shot snapshots.

The discharge can be ignited over a quite large range of the cone base to glass plate (cbgp) gap from a few tens of micrometers to more than one mm as shown in Figure 3a. The best operation and spreading of the discharge over the glass plate is nevertheless achieved from about 0.1 to 1 mm. For the higher cbgp gaps, as argon flows from the cone base to the ambient air and is less confined inside the funnel, the discharge spreading over the glass plate is compromised as shown for the 1.2 mm cbgp gap. For too small cbgp gaps, it is speculated that not enough ambient air is entering the cone, so that the discharge occurs in more “pure” argon, and then tends to contract in a single filament. More work is needed to confirm the influence of argon mixing with the ambient air or the gas depletion effect for very small gaps between the funnel and the glass plate. It was noticed that the “best” cbgp gap can be easily experimentally adjusted with simultaneously monitoring the strong peak current amplitude. This latter has the higher amplitude for a set of voltage and pulse repetition rate, when the gap is optimum.

As shown in Figure3a for different cbgp gaps, the corona discharge ignites at the needle tip and then connects to the lateral cone surface across a streamer channel at random position. As it can be seen in Figure 3b, if the peak voltage is kept constant while the pulse repetition rate is increased,

the streamer channel ignited at the tip of the needle is longer. This results that the streamer channel gradually no more randomly connects to the lateral surface and slides all along this latter down to the cone base but extends from the needle tip before connecting to the lateral surface. A main single streamer channel is observed. This latter either directly slides along the lateral surface or connects to the cone base. Some secondary streamer channels develop as secondary branches from this high intensity main channel. This shift from the diffuse and random streamer channels sliding along the cone surface to the single channel development as the pulse repetition rate is increased is likely associated with the gradual increase of the preionization level from pulse to pulse. The pulse repetition rate increase is not the best option to achieve a quite homogenous spreading of the discharge over the bottom plate except if the peak voltage is simultaneously reduced to keep the multifilament development of the discharge.

As mentioned in the introduction, the main motivation for the funnel device development is to generate a large surface plasma for biomedical applications. In most situations, biomedical applications - *in vitro* or *in vivo* and either through the so-called direct delivery of the plasma to the sample or for the indirect plasma treatment of liquid solutions - require the interaction with a more or less electrically conductive target. While the funnel operation to treat dielectric and polymer was recently successfully reported [34, 36], the insertion of liquid solution and/or conductive samples like agar plate, inside the funnel unfortunately results in the transition from the surface discharge to a transient arc having both very limited surface and driving strong current leading to dramatic temperature increase. Facing such limitations, the funnel device was implemented in this work with an additional metallic grid set with a small gap with respect to the glass plate to generate a dielectric barrier discharge in the ambient air as sketched in Figure 1b-d. The idea and innovation was to generate such DBD discharge over a large surface but potentially for a low power input considering that the powered electrode will consist of a plasma sliding discharge on the top of the glass plate. This transient electrode, consisting in the plasma filaments covering the upper surface of the glass plate is called the “plasma electrode” in the following. Such topology should differ from the more conventional DBD device where one or both electrodes consists of a large surface “solid” metallic plate. One may expect that the “plasma electrode” DBD will have a lower capacitive coupling than that of a solid DBD, eventually leading to a lower power consumption while generating a DBD over a large surface. The “plasma electrode” is both temporally transient, being generated only during some phase of the voltage pulse application, as described by the time-resolved ICCD imaging experiments reported beforehand, but also spatially transient as the plasma propagates along the glass plate.

III-1 b Funnel - DBD device

The funnel-DBD device consists in the same funnel setup reported in the previous section with the additional implementation of a grounded ring shaped grid set 1 mm apart from the outer side of the glass plate. The first experiments were performed with the same 1 mm thick borosilicate glass plate used for the funnel setup. As one key question was to characterize the generation of the air DBD, an opaque 2.8 mm thick soldering glass was used instead of the 1 mm thick glass plate to allow for the end-on ICCD imaging of the DBD only. With the transparent glass plate, the strong light emission from the argon plasma inside the funnel prevents the selective imaging of the air DBD plasma.

The insertion of the grounded metallic grid does not prevent the generation of the argon plasma inside the funnel. In that case, the surface discharge above the glass plate was observed even for small needle tip to glass plate gaps and even for high repetition rate. While for the funnel device as mentioned before, that gap decrease and pulse repetition rate increase lead to the generation of strong streamer current and a reduced glass plate plasma covering, the addition of the grounded grid 1 mm away from the bottom face of the glass plate do not impose such limitations. Drastic modification of the current waveform measured across the 100 Ω resistor connected in series with the grounded grid was also measured. As reported in Figure 4a, for the needle tip to glass plate gap of 16 mm and a pulse repetition rate of 8 kHz, the plasma ignites around 200 ns as a needle corona discharge, and rapidly reaches the glass plate when the strongest current peak is measured around 800 ns. Conversely to the situation with the funnel device alone, this strong current peak is not followed by a negative current component but by a delayed second current peak as shown around 1700 ns in Figure 4. Then during the end of the positive voltage phase a negative current component develops peaking around 3000 ns before the voltage turns to negative and a final long lasting negative current is measured from 4000 ns to about 10 µs.

Again, the time-resolved ICCD imaging both from inside the funnel and of the air-DBD plasma helps to understand the discharge development.

a)

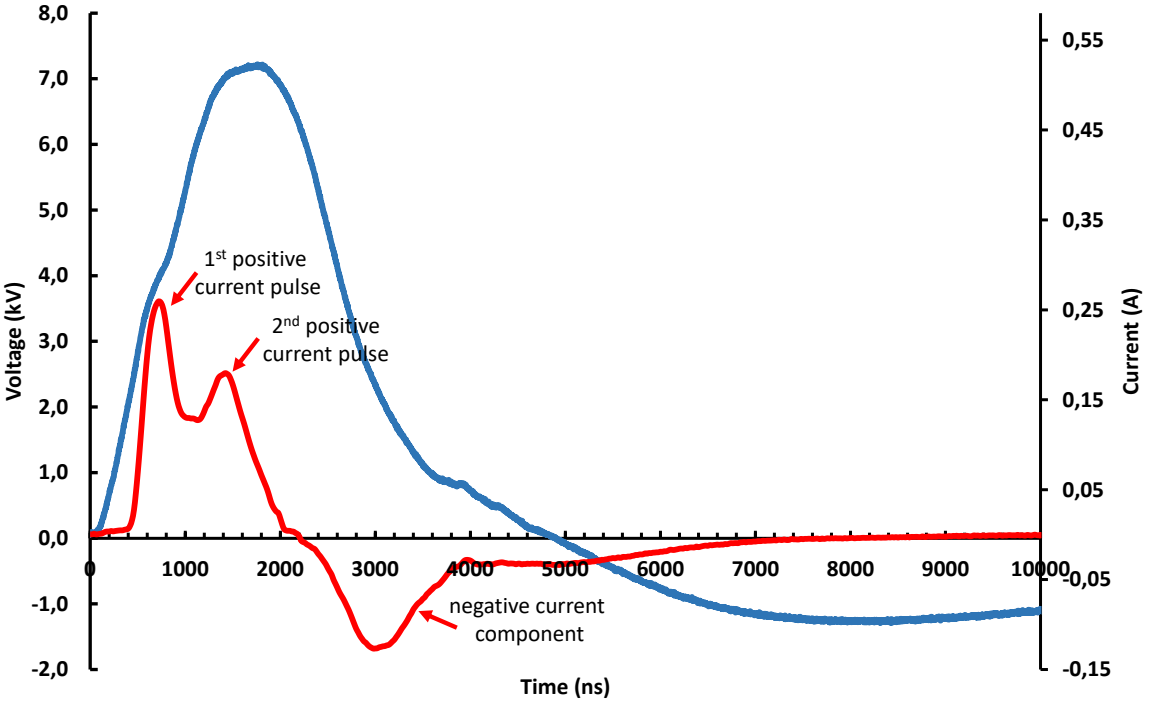
8,0
7,0
6,0
5,0
4,0
3,0
2,0
1,0
0,0
-1,0
-2,0
Voltage (kV)
0,55
0,45
0,35
0,25
0,15
0,05
-0,05
-0,15
Current (A)
0
1000
2000
3000
4000
5000
6000
7000
8000
9000
10000
Time (ns)
1st positive current pulse
2nd positive current pulse
negative current component

b)

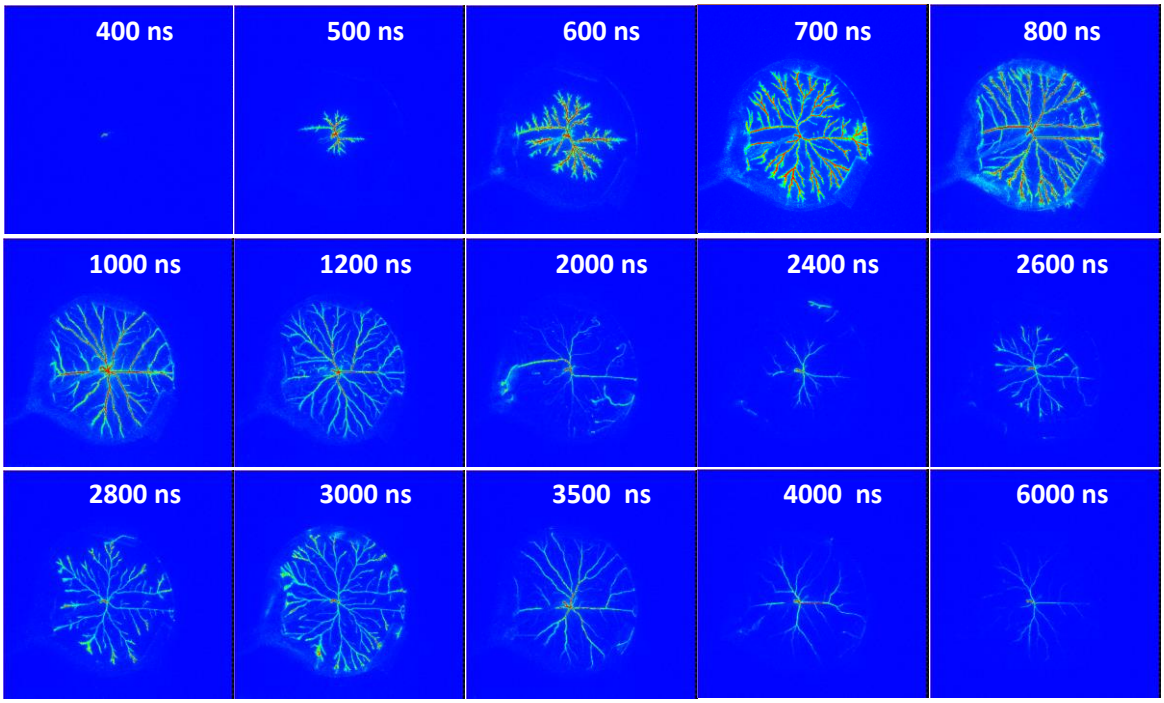
400 ns
500 ns
600 ns
700 ns
800 ns
1000 ns
1200 ns
2000 ns
2400 ns
2600 ns
2800 ns
3000 ns
3500 ns
4000 ns
6000 ns

c)

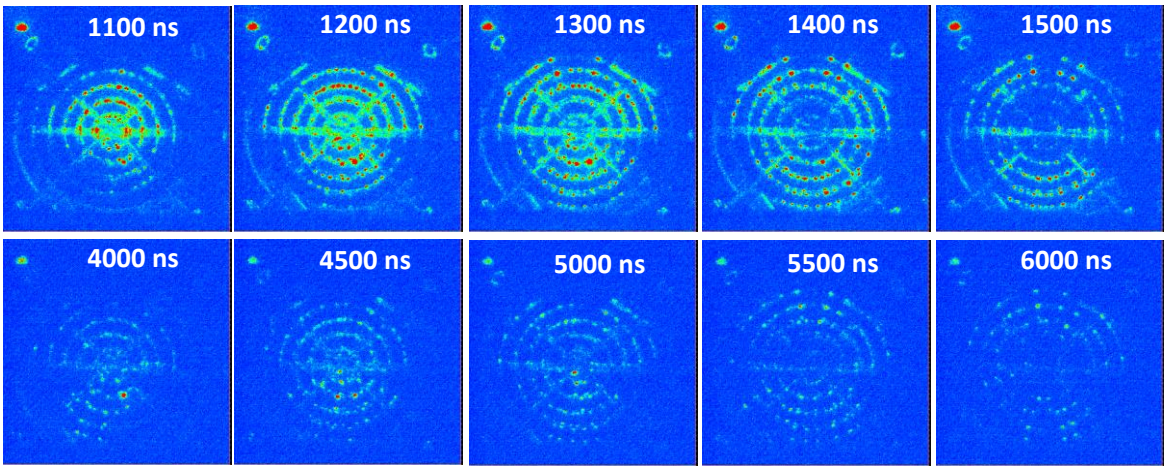

Figure 4: (a) Voltage current waveforms; (b) time-resolved ICCD imaging of the argon discharge development inside the funnel; (c) Time-resolved ICCD imaging of the air DBD between the glass and the metallic grid. The timing of each frame is expressed in ns, gating time is 50 ns, single shot acquisition for Figure 4b, image averaging over 50 shots for Figure 4c.

At about 400 ns, the needle corona is observed with the ICCD camera. From the current waveform, it can be deduced that plasma even ignites a little bit earlier. As the needle tip to the glass surface is only 16 mm, and as the voltage pulse is the same as for the funnel device, one may expect that the propagation time to the glass plate should be around 150 ns. It is indeed measured that the plasma touches the glass plate at a delay of 500 ns. Then the plasma expands over the glass plate with a very branched pattern and reaches the external boundary of the area delimited by the funnel aperture at about 800 ns in coincidence with the peak of the first strong current component. Inside the funnel, the discharge then gradually vanishes being the less emissive at about 2400 ns. Conversely to the measurement with the funnel only setup (i.e. with no air gap between the glass plate and the metallic plate), no negative current peak follows this first strong current peak. As the charging of the bottom plate will lead to the ignition of the DBD discharge, no compensation of the plate charging occurs. The second current peak shown in Figure 4a) is indeed not associated with discharge development inside the funnel but corresponds to the generation of the air-DBD as documented in Figure 4c. The spot-like generation of DBD streamer in ambient air, mainly below the grid surface is shown in Figure 4c, revealing the radial expansion of the DBD plasma from the center to the outer region of the grid vanishing before 2000 ns. Later from 2400 ns to 4000 ns, the discharge reignites inside the funnel again from the center to the outer region of the glass plate, the maximum expansion coinciding with the negative current peaking time around 3000 ns. This is a negative current phase developing while the voltage is still positive and gradually decreasing to zero at 4000 ns. This negative current, associated with a much less branching pattern of the plasma developing inside the funnel,

very likely reveals the generation of a negative streamer discharge. The charging of the bottom face of the glass plate during the previous DBD phase, probably results in the inversion of the electric field, compensating the still positive voltage applied on the needle. Not shown in this work, it was indeed measured that powering the discharge with the same shape but negative polarity voltage pulse led to the development of the negative streamer discharge at the onset of the voltage pulse. This negative discharge exhibits the same, less branched plasma pattern observed previously for the positive polarity from 2400 to 4000 ns. During this time window from 2400 to 4000 ns no plasma emission is detected in the ambient air while from 4000 ns to about 6000 ns a faint DBD plasma is again generated during the negative voltage phase of very small amplitude.

It is worth noting that DBD discharge develops twice when the argon plasma vanishes but that the DBD plasma emission stops when the argon plasma is almost extinguished. During the negative voltage phase, it is indeed measured that argon plasma ends at about 6000 ns together with the DBD plasma. This confirms that the DBD occurs because of the voltage transfer from the needle tip across the argon plasma and the consecutive electric field generated across the air gap during the inside funnel plasma generation. This is a demonstration of the DBD configuration based on a temporally and spatially transient plasma electrode.

III-1 c Electrical analysis and comparison with a classical “solid” DBD

In this section, the funnel-DBD voltage and current waveforms are analyzed for different needle tip to glass plate gaps (h). The Lissajous plots allow to assess the power coupled to the argon streamer and air DBD discharges. Fits of the Lissajous plots inspired by the work of [39] are also performed to infer the value of the different capacitances found in the discharge configuration. Features of the plasma funnel device are also compared to that of a so called “solid DBD” where the upper electrode is no more the “plasma electrode” but a conventional metallic plate (⌀5.8 cm) covering the upper surface of the glass plate, while the 1 mm air gap and the grounded grid are kept in the same configuration as with the funnel-DBD setup.

The Figure 5 presents the voltage and current waveforms measured on the grid for two (2 and 12 kHz) pulse repetition rates and for three (6, 30 and 55 mm) h values using the “plasma electrode” and the solid DBD for the same pulse repetition rates. The peak voltage amplitude of 8 kV was kept constant for all these experiments.

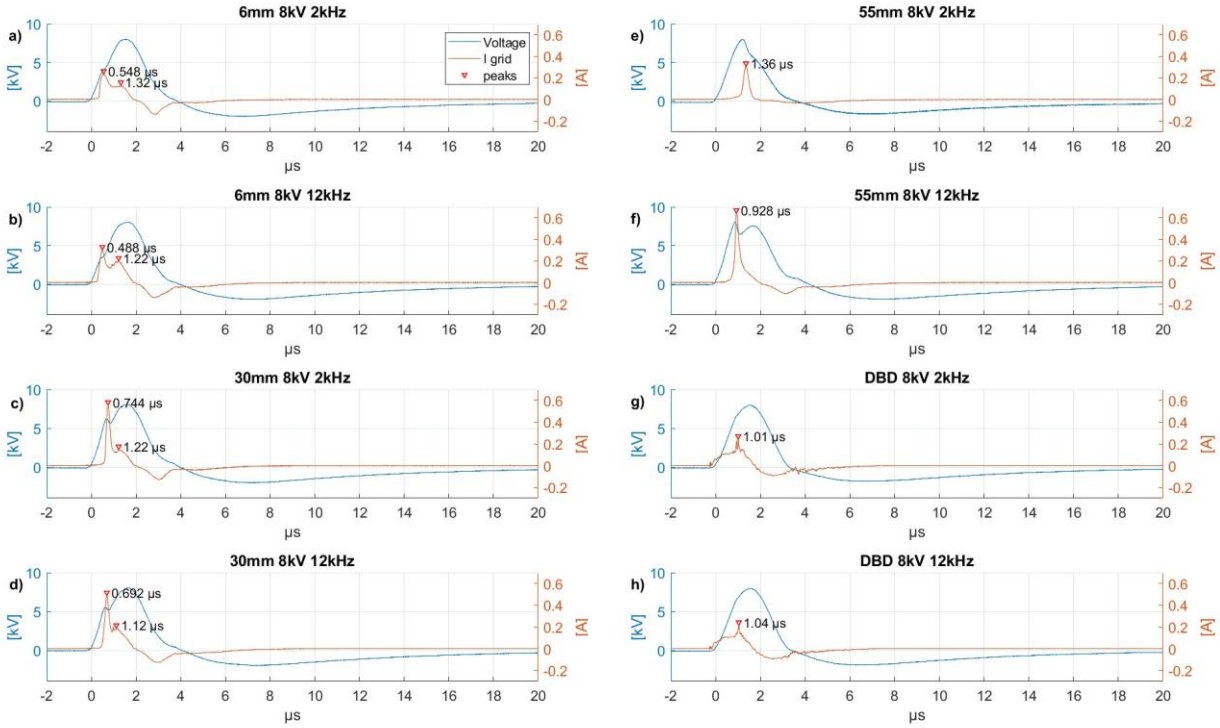

Figure 5: Voltage and current waveforms measured using the "plasma electrode" for two different pulse repetition rates and at different h values (a-f) and for the solid DBD configuration (g-h).

In the configuration of the "plasma electrode" setup, it is measured that the timing of the first strong current peak depends on the needle tip-glass plate gap, the smaller the gap the sooner the current peak is measured. At 6mm gap the first current peak is at 0.5 µs, for 30mm gap at 0.7 µs and for 55mm at 1µs. Thus, in first approximation, increasing the gap of 24-25mm increases the delay of 0.2µs which is consistent with the streamer propagation velocity of 1.4 10^7 cm/s recorded in section III-1a. This confirms that this peak reveals the streamer propagation from the needle tip to the glass plate. The peak amplitude of this high current component increases with the needle to glass plate gap increase which correlates with the higher instantaneous voltage amplitude as plasma streamer touches glass plate later with respect to the voltage onset. Also when increasing the pulse repetition rate, this first strong current peak appears sooner which is likely explained by the faster streamer propagation due to higher preionization level remaining when the pulse repetition rate is increased. Obviously, this first current pulse is not generated for the solid DBD configuration which instead presents a classic displacement current curve as the voltage increases. As discussed in the previous section on the funnel-DBD device, the second current peak originates from the air DBD plasma generation. This second peak appears from 1.1 to 1.3 µs after voltage pulse onset for the two smaller needle tip to glass plate gaps. For the 55 mm case, the two current peaks actually merge as a single one always around the time of 0.9 – 1.3 µs. This is in agreement with the peak detected for the solid

DBD at 1µs. In an experiment where the grid was set with a smallest gap with respect to the glass plate, the DBD peaks were measured at shorter delays. Conversely, if this gap is increased, the DBD peaks will appear later. Therefore, the delay is associated with the DBD streamer propagation from the grid to the glass plate.

Figure 5 also confirms that with the solid DBD, a much stronger displacement (polarization) current is generated in comparison with the "plasma electrode" setup. Again, the main reason for this is explained by the transient and smaller surface of the plasma electrode than that of a full 5.6 cm in diameter metallic plate powered all along the voltage pulse duration. The Lissajous curve analysis documented in Figure 6 also confirms the different capacitance of the two devices together with some differences in the breakdown voltage.

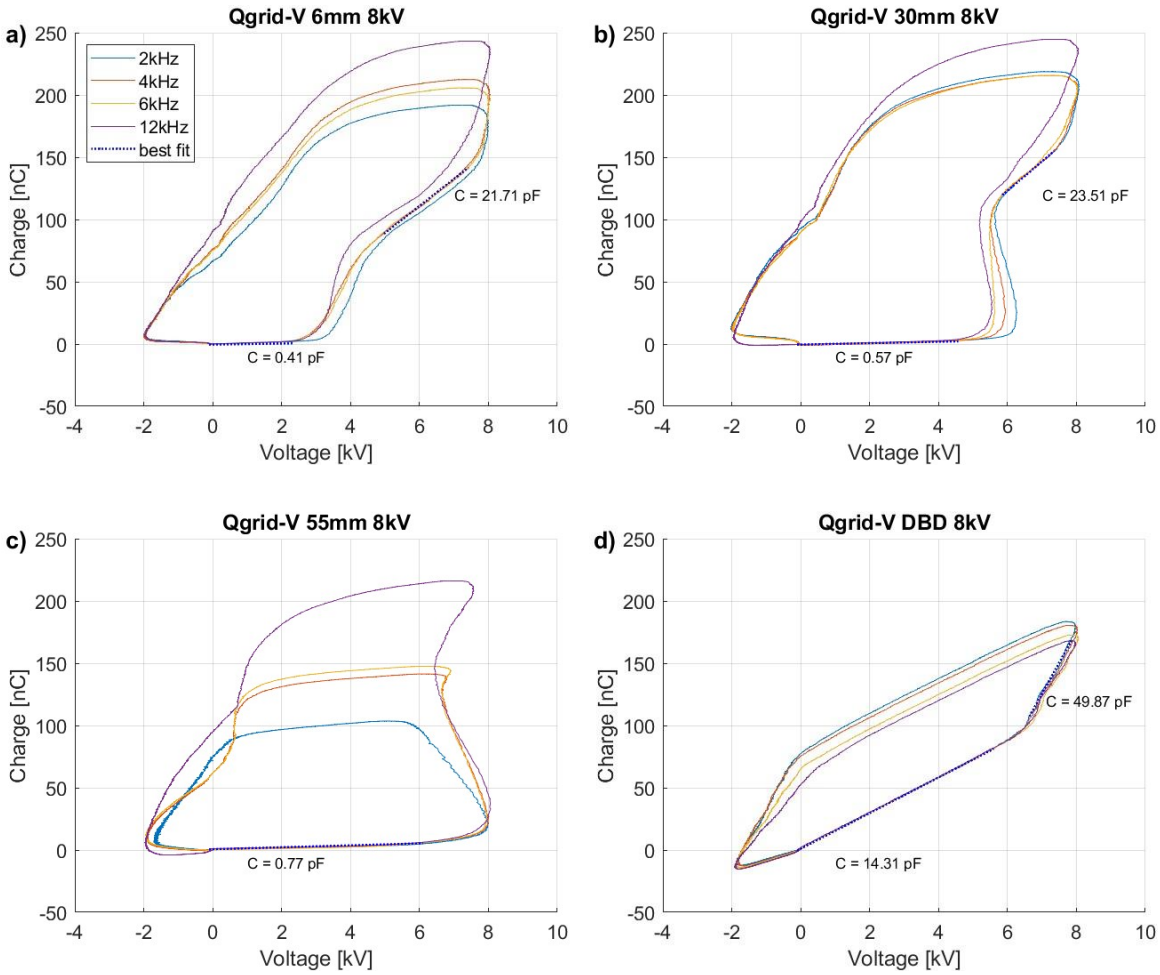

Figure 6: Lissajous figures obtained for the funnel-DBD, with plasma electrode, for different h values (a-c) and also for the solid DBD configuration (d). The operating frequencies and the measured capacitance values are displayed in the plots.

Figure 6 shows the Lissajous figures obtained on the grid electrode for the different cases. The 6 mm and 30 mm cases result relatively similar between them. All of them present a relatively horizontal base that is due to the low capacitance of the system before the generation of plasma in the funnel. The flat base of the figure is wider for the 33 mm case than the 6 mm case because the voltage required to ignite the plasma is higher. For the same reason the flat base results shorter at higher frequencies as the residual charges in the funnel atmosphere may reduce the voltage required to start the discharge. For the same reason the 55mm case has an even wider base of the Lissajous figure while the DBD configuration doesn't have a flat base but a tilted one as typical of a capacitor. This is in agreement with the values of capacitance esteemed from the slope of the Lissajous figures that show a significantly higher capacitance for the solid DBD configuration.

From Figure 6, it is measured that the voltage required to ignite the discharge is considerably lower when using the "plasma electrode". For d = 6 mm and V_{peak} = 8 kV, the discharge ignites with less than 4 kV against ~6.8 kV for the solid electrode, for the same V_{peak} set at the pulse power supply. It has to be mentioned that the minimum V_{peak} value for starting a discharge with the "plasma electrode" is 4 kV, which is related to the voltage required to ignite the discharge in argon.

From Figure 6 it can also be seen that the C_{g+d} value increases (from 0.41 to 0.77 pF) when needle to glass plate increases. The C_{g+d} values, slope of the base of the Lissajous figures, obtained with the plasma electrode are considerably lower than the one obtained for the solid DBD. Thus, the solid DBD Lissajous plot shows a charging of the capacitance characterizing the DBD reactor before the breakdown. This phase is negligible in the case of the funnel reactor because before breakdown the capacitance of the system is very low and the system is close to an open circuit.

Since the Lissajous figure obtained for the solid electrode is very close to a parallelogram, the slope of the line segment from ~6.8 kV to ~7.9 kV can be used to estimate the dielectric capacitance (C_d). This C_d value is close to 50 pF while the theoretical value (for a parallel plate capacitor) should be about 43 pF for a solid electrode with 5 cm in diameter, a 2.8 mm thick glass dielectric capacitor with and a dielectric permittivity equal to 5. Please note that the dielectric permittivity value of the glass was not experimentally checked but considered from the material datasheet. For solid DBD configuration, C_g(air) and C_d are capacitances in series having an equivalent capacitance of 14 pF (Figure 6d). Then as C_g^{-1} = (14 pF)$^{-1}$ – (50 pF)$^{-1}$, it results that C_g(air) is about 19 pF. This value corresponds to a gap height (h_g) equal to: $h_g = 8.85\times10^{-12}\times\pi\times(5.6\times10\text{-}2)^2/(19\times10^{-12})$ = 1.15 mm which is consistent with the 1 mm glass plate - grid gap set during the experiments.

For funnel-DBD configuration $C_{g(Ar)}$, C_d and $C_{g(Air)}$ are in series. From Figures 6a and 6b, C_d is about 23 pF:

- It can be noticed that this straight portion of the Lissajous plot appears after the first current peak, meaning the argon discharge reaches the glass plate, and right before the DBD current is detected. This is the time where the dielectric is polarized by the voltage applied from the needle electrode to the glass plate surface across the argon plasma.
- As the C_d decreases from 50 to 23 pF when turning from solid DBD, operated with a 5.6 in diameter metallic electrode, to the plasma electrode DBD, it can be estimated that the "active surface" of the plasma electrode is about 46%. This is qualitatively in good agreement with the ICCD measurement in Figure 4b at time 1000 ns a few tens of nanosecond before the DBD will be generated as shown in Figure 4c.

Thus, the lower C_{g+d} values obtained for the funnel-DBD are likely due to the small effective area provided by the combination of the plasma and grid electrodes.

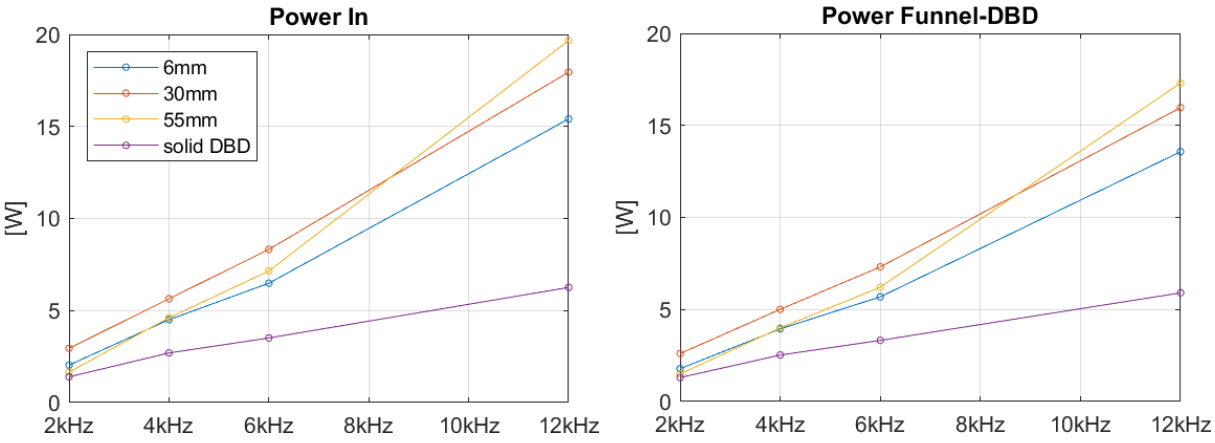

Figure 7: (Left) Total input power delivered to the reactor and (Right) power delivered to the DBD generated in air for different frequencies and different needle-glass gaps. Comparison with the solid DBD for the same operating conditions. Peak voltage is fixed at 8kV.

The Figure 7 presents the total input power to the reactor P_{in}, inferred from using the voltage measured on the needle electrode and the current from the current monitor set around the high voltage cable (see Figure 1d) and the funnel-DBD power ($P_{f\text{-}DBD}$, inferred from the Lissajous plots considering the needle voltage and current measured across the 100 Ω shunt resistor) for a constant 8 kV peak voltage amplitude but for 2, 4, 6 and 12 kHz pulse repetition rates and for 6, 30 and 55 mm needle to glass plate gaps. As expected the input power increases in any case with the pulse repetition rate. The power delivered to the funnel-DBD is slightly lower than the total input power, the difference

between the two increasing for the higher pulse repetition rates. This is likely associated with power loss in the high voltage cable, stray capacitances, joule heating, as well as in the Ar discharge. The rod and funnel temperature increases were extremely limited even for high repetition rate and for long-term operation during tens of minutes, which somehow confirms the electrical measurements. The bottom plate experienced some more significant temperature increase probably resulting from the DBD discharge ignition.

III-2 RONS generation with the funnel-DBD

As the air DBD obviously generates ozone, the ozone concentration was measured for different settings of the funnel-DBD device for three main reasons: first this species can be quite efficient for decontamination applications, second this measurement is a way to characterize the time evolution of the DBD operation, and finally its a way to estimate the influence of the injected power and power density on ozone generation. This latter parameter is known to be a key feature of any air DBD ozone generator [43]. The Figures 8a-d present the absolute and normalized time evolutions during five minutes of the evolution of the ozone concentration for two needle to glass plate gaps (6 and 30 mm) and for four pulse repetition rates (2, 4, 6 and 12 kHz). Ozone measurement started as the funnel-DBD was switched on and was sampled each 12 seconds. The air in the collecting box is continuously sucked at a flow rate of 1.5 slm, this rate was imposed by the ozone analyzer. No modification of the electrical signals, current and voltage, were observed during the ozone measurement, the waveforms being exactly the same as when the collecting box was not used. This is an indirect indication that the ozone accumulation in the box is not an issue, and that the funnel-DBD discharge operates identically with or without the collecting box. In any operating conditions, the ozone concentration increases during the first tens of seconds of operation. This is the time needed to reach the equilibrium between the gas collecting box and the sampling cell of the ozone analyzer. The same one minute time delay was also measured for the ozone concentration to come back to zero as the discharge was switched off while the ozone sampling was kept constant at 1.5 slm.

For the 6 mm gap and 2 kHz operation the steady state ozone concentration of around 80 ppm is reached, and remains relatively stable, about 4 minutes after the funnel-DBD ignition. For higher repetition rates, the maximum or steady state concentration is measured after one minute. The 4 kHz operation generates a quite steady 100 ppm ozone concentration, while the 6 kHz regime results in 80 ppm and a slightly decreasing level over 5 minutes. For the 12 kHz operation, the maximum ozone concentration is reduced to 60 ppm and rapidly decreases after one minute being one half (30 ppm) after 2 minutes of operation. The same trends and ozone levels are measured for the 30 mm gap, with

the exception that even for the 2 kHz operation the ozone maximum is reached after one minute as for any other pulse repetition rates.

The surface covered by the DBD is estimated from the ICCD images showing that the DBD occurs as plasma spots along the grid rings having a diameter of about 2 mm. The area of the DBD is therefore estimated to be 8cm^2. The Figure 8e plots the power density for the 6 and 30 mm needle to glass plate gaps, for 2, 4, 6 and 12 kHz repetition rates.

As reported in [43], the ozone generation with conventional air DBD gradually shifts from the ozone to the NOx regime when surface power density (SPD) increases above ~0.3 W/cm^2. For SPD values higher than this threshold the phenomenon of ozone quenching is observed and the ozone concentration is rapidly reduced due to chain reactions with NOx molecules. It appears that the same behavior is measured with the funnel-DBD device. The lowest SPD value recorded, 0.22 W/cm^2, is for the 6mm case at 2kHz. As expected this condition shows an increasing ozone concentration trend, not affected by ozone quenching. The case at 30mm and 2 kHz has an SPD of 0.32 W/cm^2, very close to the threshold, and presents a transition regime where the ozone concentration slowly decreases. All the other investigated cases are instead in the NOx regime and favor the production of NOx molecules over ozone production. Even if the NOx concentrations were not measured in the present work, test strips measurement of nitrite and nitrate when a water solution was exposed to the funnel-DBD effluent for a few minutes indeed reveals that the more NOx were detected in water when increasing the pulse repetition rate from 1 to 8 kHz. This confirms the increasing generation of NOx simultaneously with the decreasing of ozone production with the funnel-DBD setup when the pulse repetition rate, and associated power density, is increased. It is worth mentioning that almost no H_2O_2 was detected during the experiments that were carried out in this work. If compared with the classic solid DBD configuration it is easily observed that the funnel-DBD allows to cover a much larger range of SPD values varying the repetition frequency. This could be of interest for applications where high versatility is required or high values of SPD are necessary.

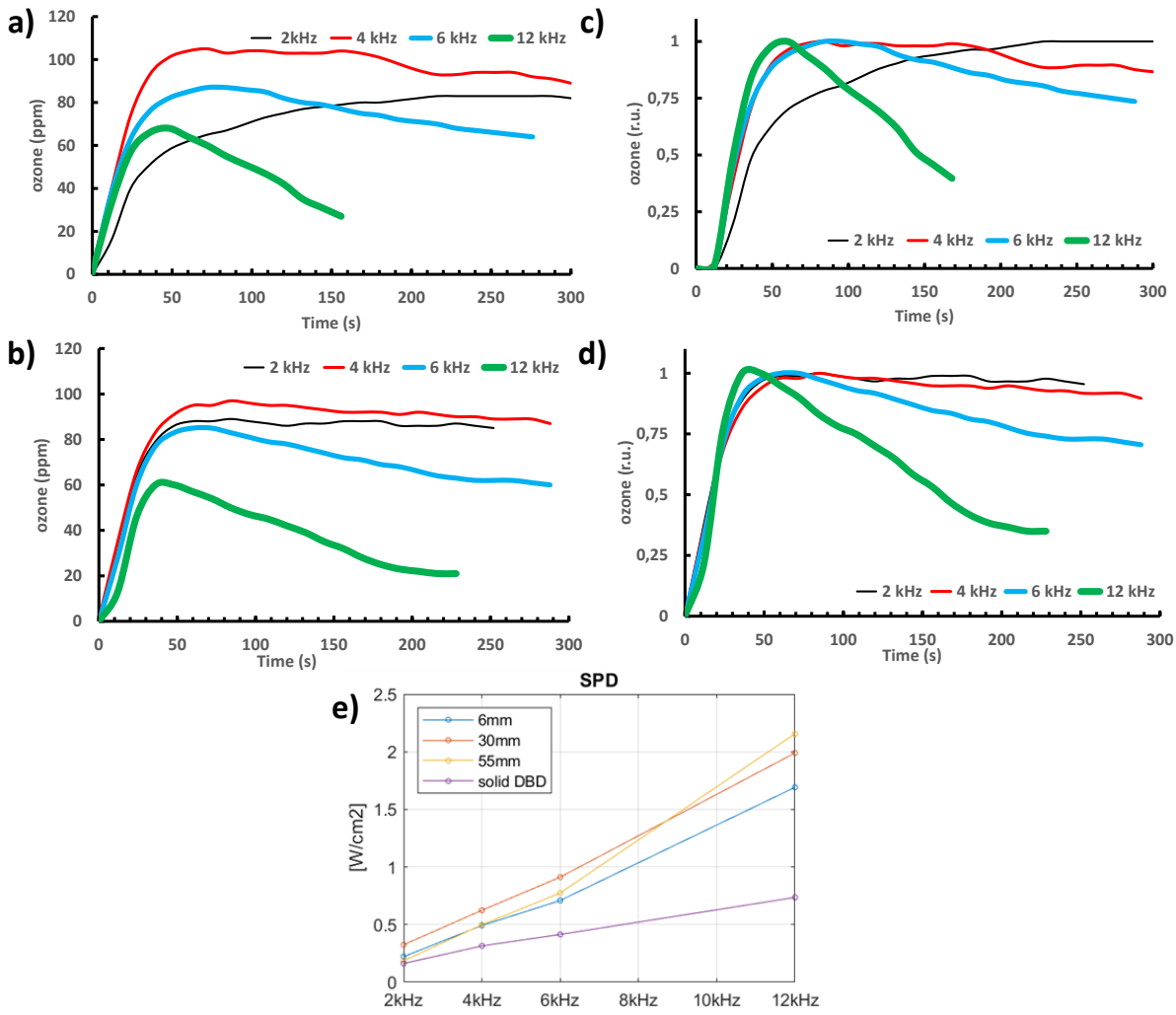

Figure 8 a) Time evolution of ozone concentration for a) 6 mm and b) 30 mm gap with pulse repetition ranging from 2 to 12 kHz. b) and d) plots the same but normalized data. e) Surface power density evolution with the pulse repetition rate for the funnel-DBD for three different needle tip to glass plate gaps and for solid DBD configuration.

III-3 Funnel-DBD potentialities for biological decontamination

III-3a Assays with KI-starch agar and *E. coli*

Preliminary tests using KI-starch agar and a bacteria (*E. coli*) were carried out in order to evaluate the potential of funnel-DBD device for large surface treatment and inactivation of microorganisms exposed to indirect plasma treatment. Figure 9 shows results obtained for (a) KI-starch agar and (b) *E. coli*. The first Petri dish was treated using the small funnel and the second one with the big funnel. The small funnel has an opening of 80 mm in diameter while the big funnel has an opening

of 130 mm in diameter. In both cases, the exposure time was 60 seconds. As it can be seen in Figure 9a, the entire Petri dish with KI-starch agar reacted to the indirect exposure to the plasma treatment. It can be noticed that the distribution of reactive species over the surface is more homogeneous within a radius of ~2.5 cm from the center of the sample, with decreasing intensity towards the edges.

(a) KI-Starch agar - 60 s exposure (b) *E. coli* - 60 s exposure

Figure 9: Results of indirect exposure to the plasma produced by the funnel-DBD device for: (a) KI-starch agar and (b) *E. coli*.

Regarding the results of *E. coli* treatment, it can be seen in Figure 9b that the decontamination effects can be seen over most of the sample's surface, with reasonable homogeneity, compared to the control sample where a complete monolayer of bacterial structure was formed over the whole area of the Petri dish. It can be noticed that the plasma treatment did not form an inhibition zone with circular pattern, as in the case of the sample with KI starch. After a short treatment time (60s) no full decontamination is achieved but a significant microbial reduction on the whole area of the Petri dish.

III-3b Assays for yeast: *C. glabrata*

In the post- treatment cultivation, areas with no microbial growth were formed. These were recognized as inhibition zones in the Petri dish. The dependence of inhibition efficiency is directly related to the discharge power and the treatment time. With a longer treatment time, the inhibition efficiency increased sharply, as it can be seen in Figure 10.

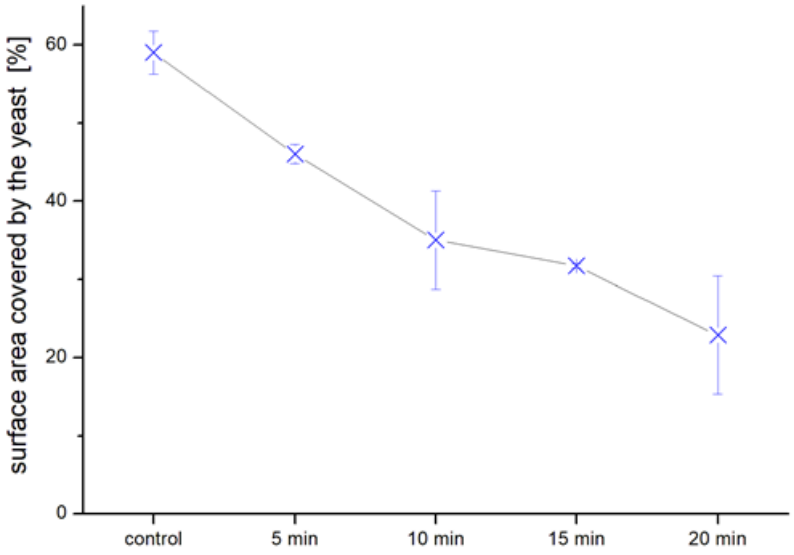

Figure 10: Decrease in microbial growth with the increasing treatment time using the big funnel set- up and 8.6 kV peak voltage.

When comparing the inhibition efficiency of the two tested set-ups with different sizes of funnels, we can see that similar efficiency is obtained when using the small funnel with smaller voltage and the big funnel with higher voltage. This is caused by a similar distribution of active species in the discharge area. Taking into consideration that the small funnel covers smaller area, thus smaller voltage is enough to produce similar power densities, which results in similar concentrations of active species per area. This trend can be seen in Figure 11.

Regarding the time stability of the inhibited area, from the results shown in Figure 11 we may conclude that the difference between the area inhibited after 24 h and 1 week time is negligible. Small overgrowth from the edge zones was caused by the proliferation of the vital cells from the border of the inhibited area. But this difference was no more than 5 % and no new colonies were formed in the decontaminated area. Thus, we can conclude that the inhibited area remains stable over a period of time. This fact may be very beneficial for example in the food industry where products or surfaces need to remain decontaminated for a long period of time.

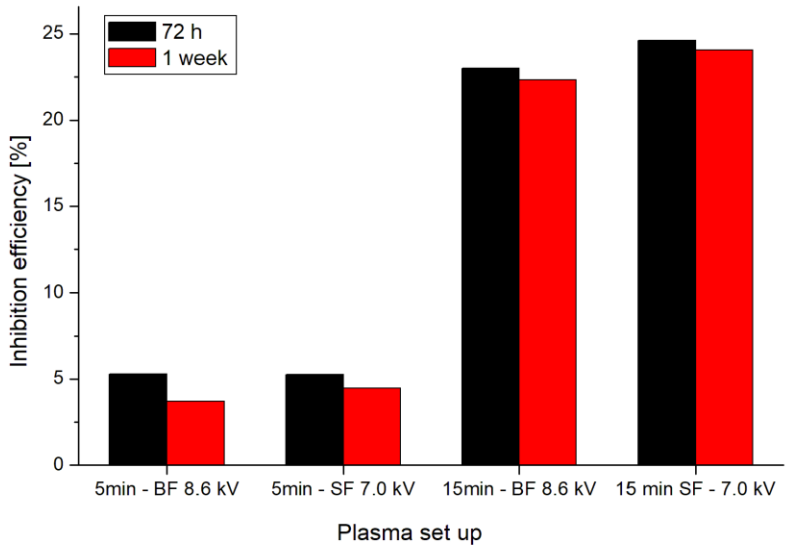

Figure 11: Comparison of inhibition efficiency 72 hours and one week after the plasma treatment for two different treatment times with the small funnel (SF) and big funnel (BF) set-ups.

IV Conclusion/perspectives

In this work a funnel-based plasma source was investigated in two different configurations: the sole funnel and the funnel-DBD. In the former, the discharge propagates over the inner wall of the funnel and spreads out over the cone base dielectric surface. The funnel-DBD device is a modified version of the first configuration that makes use of the discharge inside the funnel to produce a DBD plasma in the air gap between a dielectric plate and a metallic grid placed below the funnel. The latter setup generates an air DBD with a specific configuration. While the glass dielectric and grounded grid are commonly used to generate DBD, the funnel-DBD setup operates with a powered electrode being the plasma that acts as a virtual cathode/anode. Both configurations have the potential to be used for the treatment of large area surfaces. However, the sole funnel configuration is not suitable for treating conductive materials/surfaces since this would result in a transition from the surface discharge to a transient arc towards the target. The proof of concept for the air-DBD plasma generation and its likely potentialities for large surface decontamination in the funnel-DBD configuration are reported for the first time in this work.

Time-resolved ICCD imaging diagnostic and electrical measurements revealed that in both configurations the discharge development inside the funnel, as well as in the glass-grid gap is linked to the electrical current that flows through the system. However, fundamental differences were found regarding the behavior of the discharge current measured with each configuration. In the funnel alone,

the discharge current presents a positive peak followed by a negative one, both strong and narrow, where the latter follows the plasma sliding phase on the glass plate. In the funnel-DBD case, the current waveform tends to present two narrow positive current peaks before a negative current phase. By comparing the current waveforms it can also be seen that the duration of the plasma discharge in the funnel-DBD is much longer than in the funnel alone. The air DBD is first generated following the charging on the inside funnel base plate though the argon discharge. Then it radially expands from the center to the outer boundary of the grid electrode and vanishes a few hundreds of nanoseconds later as the current turns to zero. Ensuing the air DBD expansion, the bottom surface of the glass plate is charged by the streamer propagation to this surface. This induces that the Laplacian field imposed by the positive voltage still applied from the needle tip of the funnel, which is screened by the electrical field across the glass plate. As a result, a negative streamer discharge occurs in the funnel exhibiting a much less branched pattern than that imaged during the early stage positive streamer generation, as previously reported for pin to plate argon discharge at atmospheric pressure [42]. During the low amplitude negative voltage phase, the air DBD plasma ignites for a second time but with a much lower intensity.

A comparison between the DBD with plasma electrode and one with a solid electrode revealed that the capacitance due to the gas gap plus dielectric barrier (C_{g+d}) is much lower with the funnel-DBD setup than with the standard solid DBD configuration. This is probably the reason for the reduction in the voltage required to ignite the DBD discharge in the glass-grid air gap. The lower C_{g+d} values obtained with the plasma electrode also resulted in the reduction of the displacement current. This is an important point, since it can lead to an opportunity for using fragile and thin materials as dielectric barriers. It was also found that funnel-DBD with the plasma electrode provides a higher surface power density when compared to the solid electrode DBD for the same input voltage, which can lead to a more efficient treatment. Future work and optimization can be envisioned at least in two ways. First with improving the argon discharge efficiency with gas admixtures or by delivering voltage pulse of both positive and negative polarities with various duty cycles. Second, the nature and dielectric permittivity of the DBD barrier may be investigated to improve the air-DBD efficiency.

Preliminary assessments on surface decontamination revealed that the funnel-DBD device can be used for such purposes. A good antimicrobial efficacy, over a relatively large surface area, has been demonstrated for indirect exposure of *E. coli* and *C. glabrata* to the plasma produced by the device. The increase in the inhibition efficiency with treatment time, as observed with *C. glabrata* combined with the reduction in ozone production with device operating time indicates that the inhibition efficiency of the plasma is not likely caused only by the exposure to ozone, but also to other reactive

species, probably nitrites and nitrates, produced in the discharge. The biological assays also revealed a device scaling potential through the use of funnels of different sizes.

Based on a recently published article about the antimycotic effects of different CAP sources tested on the same yeast strain (in similar concentrations) we are able to compare the efficiency of this novel device with other CAP sources. In the published study [44] the treatment times were much shorter (up to 1 min), thus we cannot make exact conclusions but we can try to extrapolate and make some assumptions. In case of the transient spark and the streamer corona the inhibited areas were very small (in mm^2), so these devices are not suitable for large area decontamination but rather a local treatment in medical fields. With the use of microwave discharges high efficiency is achieved after very short treatment times (1 min) but prolonged treatment times are not possible due to the temperature limits. In case of a sustained local treatment there is an accumulation of temperature around the treated spot that may lead to local overheating over time. Thus with the microwave discharges used in the study it is not possible to prolong that treatment time up to 15 min. There is also a possibility of using a programmed mover arm connected to the microwave plasma torch that can scan larger surfaces thus resulting in bigger decontamination areas without the problem of local overheating but these results have not been published yet. When comparing the funnel DBD with the MW sources it is important to mention the operating frequencies (kHz for funnel DBD vs GHz for MW sources). An important advantage of the funnel DBD is its independence on the target thanks to its separation from the treated surface itself. The discharge produced by the funnel DBD is confined between the glass and the grid thus avoiding contact with the treated object. Compared to the plasma jets or torches whose properties highly depend on the properties of the treated surface.

There is also a possibility of coupling several DBD systems to treat different objects or larger areas simultaneously which supports its matching and scalability perspectives.

Declarations

Ethical Approval
Not applicable

Competing interests
Authors have no competing interests

Authors' contributions

F.N., A.S., K.T., S.D. J.M.P., K.G.K. and E.R. performed the experimental work. F.N., A.S., K.T., J.M.P., K.G.K. and E.R wrote the main manuscript text. All authors (F.N., A.S., K.T., S.D. J.M.P., J.H., F.K., K.G.K. and E.R.) reviewed the manuscript.

Funding
KT was supported by a short term scientific mission fellowship by COST CA20114 PLASTHER. This work is supported by CNRS GDR 2025 HAPPYBIO. KGK and FN acknowledge financial support from the São Paulo Research Foundation - FAPESP under grants 2019/05856-7, 2020/09481-5 and 2021/14391-8

Availability of data and materials
All data are wiil be made available by the corresponding author upon reasonable request.

Acknowledgements

KT was supported by a short term scientific mission fellowship by the COST CA20114 PLASTHER. This work is supported by CNRS GDR 2025 HAPPYBIO. KGK and FN acknowledge financial support from the São Paulo Research Foundation - FAPESP under grants 2019/05856-7, 2020/09481-5 and 2021/14391-8. Authors express their sincere thanks to F. Brulé-Morabito (CBM, UPR4301 CNRS Orleans) for her invaluable help in the design and implementation of biological assays.

References

[1] Winter J, Brandenburg R, Weltmann K-D (2015) Atmospheric pressure plasma jets: an overview of devices and new directions. Plasma Sources Sci Technol 24: 064001

[2] Robert E, Sarron V, Ries D, Dozias S, Vandamme M, Pouvesle J M (2012) Characterization of pulsed atmospheric-pressure plasma streams (PAPS) generated by a plasma gun. Plasma Sources Sci Technol 21 (3):034017

[3] Viegas P, Slikboer E, Bonaventura Z, Guitella O, Sobota A, Bourdon A (2022) Physics of plasma jets and interaction with surfaces: review on modeling and experiments. Plasma Sources Sci Technol 31: 053001

[4] Ma C, Nikiforov A, Hegemann D, De Geyter N, Morent R, Ostrikov K (2023) Plasma-controlled surface wettability: recent advances and future applications. Int Mat Rev 68(1): 82-119

[5] Corbella C, Portal S, Keidar M (2023) Flexible cold atmospheric plasma jet sources. Plasma 6: 72-88

[6] Cho G, Kim Y, Uhm HS (2016) The jet-stream channels of gas and plasma in atmospheric-pressure plasma jets. J Korean Phys Soc 69(4): 525-535

[7] Yamamoto A, Kawano Y, Nakai M, Nokagawa T, Sakugawa T, Hosseini H, Akiyama H (2015) Investigation of gas flow dependence of plasma jet produced pulsed power. IEEE Trans Plasma Sci 43(10): 3451-3455

[8] Birer Ö, (2015) Reactivity zones around an atmospheric pressure plasma jet. Appl Surf Sci 354: 420-428

[9] Kostov KG, Nishime TMC, Castro AHR, Toth A, Hein LRO (2014) Surface modification of polymeric materials by cold atmospheric plasma jet. Appl Surf Sci 314: 367-375

[10] Nishime TMC, Wagner R, Kostov KG (2020) Study of modified area of polymer samples exposed to a he atmospheric pressure plasma jet using different treatment conditions. Polymers 12(5):1028-1046

[11] Nascimento F, Leal BS, Quade A, Kostov K (2022) Different radial modification profiles observed on APPJ-treated polypropylene surfaces according to the distance between plasma outlet and target. Polymers 14: 4524-4540

[12] Narimisa M, Onyshchenko Y, Morent R, De Geyter N (2021) Improvement of PET surface modification using an atmospheric pressure plasma jet with different shielding gases Polymers 215: 123421

[13] Li H, Li M, Zhu H, Zhang Y, Du X, Chen Z, Xiao W, Liu K, (2022) Realizing high efficiency and large-area sterilization by a rotating plasma jet device. Plasma Sci Technol 24: 045501

[14] Lv X, Ren RC, Ma T, Feng Y, Wang D (2012) An atmospheric large-scale cold plasma jet. Plasma Sci Technol 14(9): 799-801

[15] Wu K, Liu J, Wu J, Chen M, Ran J, Pang X, Jia P, Li X, Ren C (2023) A double-mode planar argon plume produced by varying the distance from an atmospheric pressure plasma jet. High Voltage 8(3): 1-7

[16] Zhang X, Jin C, Zhuge L, Wu X (2020) Hydrophilicity improvement of quartz glass surface by a large-area atmospheric pressure plasma generator. IEEE Trans Plasma Sci 48(3): 692-699

[17] Tudoran CD, Coros M. (2022) Design and construction of new plasma applicator for the improved disinfection and activation of large surfaces. Plasma 5: 436-450

[18] Polášková K, Nečas D, Dostái L, Klíma M, Fiala P, Zajíčková L (2022) Self-organization phenomena in cold atmospheric pressure plasma slit jet. Plasma Sources Sci Technol 31: 125014

[19] Li H-P, Nie Q-Y, Yang A, Wang Z-B, Bao C-Y (2014) An atmospheric cold plasma jet with a good uniformity, robust stability, and high intensity over aa large area. IEEE Trans Plasma Sci 42(10): 2470-2471

[20] O'Neill FT, Twomey B, Law VJ, Milosavljevic V, Kong MG, Anghel SD, Dowling DP (2012) Generation of active species in a large atmospheric-pressure plasma jet. IEEE Trans Plasma Sci 40(11): 2994-3002

[21] Baldanov BB (2022) Experimental study of the effect of a nonthermal plasma jet on the wettability of polytetrafluoroethylene surface. Plasma Chemistry 56(3): 240-244

[22] O'Connor N, Humphreys H, Daniels S (2014) Cooperative merging of atmospheric pressure plasma jets. IEEE Trans Plasma Sci 42(3): 756-758

[23] Nizard H, Gaudy T, Toutant A, Iacono J, Descamps P, Leempoel P, Massines F (2015) Influence of discharge and jet flow coupling on atmospheric pressure plasma homogeneity. J Phys D: Appl Phys 48: 415204

[24] Johnson MJ, Boris DR, Petrova TB, Walton SG (2020) Extending the volume of atmospheric pressure jets through the use of additional helium gas streams. Plasma Sources Sci Technol 29: 015006

[25] Omran AV, Busco G, Ridou L, Dozias S, Grillon C, Pouvesle J-M, Robert E (2020) Cold atmospheric single plasma jet RONS delivery on large biological surface. Plasma Sources Sci Technol 29: 105002

[26] Wang S, Zhang J, Li G, Wang D (2014) Cold large-diameter jet near atmospheric pressure via a triple electrode configuration. Vacuum 101: 317-320

[27] Liu F, Zhang B, Fang Z, Wan M, Wan H, Ostrikov K (2017) Jet-to-jet interactions in atmospheric-pressure plasma jet arrays for surface processing. Plasma Process Polym 15: e1700114

[28] Ghasemi M, Olszewski P, Bradley JW, Walsh JL (2013) Interaction of multiple plasma plumes in an atmospheric pressure jet array. J Phys D: Appl Phys 46: 052001

[29] Fang Z, Ding Z, Shao T, Zhang C (2016) Hydrophobic surface modification of epoxy resin using an atmospheric pressure plasma jet array. IEEE Trans Dielec Elect. Insulation 23(4): 2288-2293

[30] Cao Z, Nie Q, Bayliss DL, Walsh JL, Ren CS, Wang DZ, Kong MG (2010) Spatially extended atmospheric plasam arrays. Plasma Sources Sci Technol 19: 025003

[31] Ma S, Lee M-H, Kang SU, Lee YS, Kim C-H, Kim K (2021) Development of an atmospheric nonthermal multineedle dielectric barrier discharge jet for large area treatment of skin diseases. Current Appl Phys 24: 24-31

[32] Maho T, Binois R, Brulé-Morabito F, Demasure M, Douat C, Dozias S, Bocanegra PE, Goard I, Hocqueloux L, Helloco C, Orel I, Pouvesle J-M, Prazuck T, Stancampiano A, Tocaben C and Robert E (2021) Anti-bacterial action of plasma multi-jet in the context of chronic wound healing. Appl Sciences 11**:** 9598-9618

[33] Chimire B, Szili EJ, Short RD (2022) A conical assembly of six plasma jets for biomedical applications. Appl Phys Lett 121: 084102

[34] Mui TSM, Mota RP, Quade A, Hein LRO, Kostov KG (2018) Uniform surface modification of polyethylene terephthalate (PET) by atmospheric pressure plasma jet with a horn-like nozzle. Surf Coat Technol 352: 338-347

[35] Punith N, Singh AK, Ananthanarasimhan J, Boopathy B, Chatterjee R, Hemanth M, Chakravortty D, L. Rao L (2023) Generation of neutral pH high-strength plasma-activated water from a pin to water discharge and its bactericidal activity on multidrug-resistant pathogens. Plasma Process Polym 20: e2200133

[36] Kodaira FVP, Leal BHS, Tavares TF, Quade A, Hein LRO, Chiappim W, Kostov KG (2023) Simultaneous treatment of both sides of the polymer with a conical-shaped atmospheric pressure plasma jet. Polymers 15(2):461-474

[37] Nishime TMC, Werner J, Wannicke N, Mui TSM, Kostov KG, Weltmann K-D, Brust H (2022) Characterization and optimization of a conical corona reactor for seed treatment of rapeseed. Appl Sciences 12(7): 3292-3306

[38] Robert E, Barbosa E, Dozias S, Vandamme M, Cachoncinlle C, Viladrosa R, Pouvesle J M (2009) Experimental study of a compact nanosecond plasma gun. Plasma process polym 6(12):795-802

[39] Pipa AV, Koskulics J, Brandenburg R, Hoder T (2008) The simplest equivalent circuit of a pulsed dielectric barrier discharge and the determination of the gas gap charge transfer. Rev Sci Instrum 83(11): 115112

[40] Catalogue of cultures MUNI SCI: Institute of experimental biology, the Czech Collection of Microorganisms (CCM) (1963) Czech Republic. https://ccm.sci.muni.cz/en. accessed on 26 of June 2023

[41] Hrudka J, Scholtz V, Jiresová J, Rácová Z, Khun J, Klenivskyi M, Machková A. (2023) Automatic image analysis of the effects of non-thermal plasma on mold growth. Proceedings of 25th International Symposium on Plasma Chemistry, Kyoto, Japan

[42] Celestin S, Allegraud K, Canes-Boussard G, Leick N, Guaitella O, Rousseau A (2012) Pattern of plasma filaments propagating on a dielectric surface. IEEE Trans Plasma Sci 36(4): 1326-1327

[43] Simoncelli E, Schulpen J, Barletta F, Laurita R, Colombo V, Nikiforov A, Gherardi M (2019). UV–VIS optical spectroscopy investigation on the kinetics of long-lived RONS produced by a surface DBD plasma source. Plasma Sources Sci Technol 28(9): 095015.

[44] Trebulová K, Krčma F, Skoumalová P, Kozáková Z, Machala Z (2023) Effects of different cold atmospheric-pressure plasma sources on the yeast *Candida glabrata.* Plasma Process Polym 20: e2300048